Research Article | Vol. 13, No. 12 / 1 Dec 2022 / Biomedical Optics Express 6182
Biomedical Optics EXPRESS

Detectability of low-oxygenated regions in human muscle tissue using near-infrared spectroscopy and phantom models

TARCISI CANTIENI,* OLIVER DA SILVA-KRESS, AND URSULA WOLF

Institute of Complementary and Integrative Medicine, University of Bern, Bern, Switzerland
*tarcisi.cantieni@unibe.ch

Abstract: The present work aims to describe the detectability limits of hypoxic regions in human muscle under moderate thicknesses of adipose tissue to serve as a groundwork for the development of a wearable device to prevent pressure injuries. The optimal source-detector distances, detection limits, and the spatial resolution of hypoxic volumes in the human muscle are calculated using finite element method-based computer simulations conducted on 3-layer tissue models. Silicone phantoms matching the simulation geometries were manufactured, and their measurement results were compared to the simulations. The simulations showed good agreement with the performed experiments. Our results show detectability of hypoxic volumes under adipose tissue thicknesses of up to 1.5 cm. The maximum tissue depth, at which hypoxic volumes could be detected was 2.8 cm. The smallest detectable hypoxic volume in our study was 1.2 cm^3. We thus show the detectability of hypoxic volumes in sizes consistent with those of early-stage pressure injury formation and, consequently, the feasibility of a device to prevent pressure injuries.

1. Introduction

Pressure injuries (PI) are a disturbingly prevalent health care problem that primarily affects persons who cannot reposition themselves, such as paraplegics (prevalence of 85% per lifetime [1]) or long-term and acute care patients (incidence of 30% and 25%, respectively [2]).

Because of the strenuous and expensive healing process of PI [3], the best treatment is prevention or early detection [4].

It has been shown that impaired oxygenation in the weight-bearing muscle tissue constitutes a significant risk factor for the development of PI [5–8]. Since it takes approximately 30 min (depending on the individual subject) before irreversible damage occurs [9] PI could effectively be prevented simply by repositioning the body and thus allowing the blood circulation to recover. However, this requires a non-invasive device that detects the impending danger of critically sub-oxygenated tissue without introducing pressure points.

This work aims at establishing a framework for such an apparatus by finding the limits of detectability of low-oxygenated regions (hypoxic volumes) within human tissue by means of near-infrared spectroscopy (NIRS). To the best of our knowledge, no comparable study has been published so far.

The primary parameters found to influence the detectability of hypoxic volumes (or bodies) besides the degree of hypoxia of the hypoxic body were the volume size and vertical positioning of the hypoxia (can be seen similarly in [10]).

Another, well-studied, parameter is the adipose tissue thickness (ATT): Various studies have striven to find, quantify or correct the influence of the ATT on the error of tissue property measurements or calculated tissue oxygen saturation [11–18]. In this work, the effect of ATT is investigated along with the depth and size of the hypoxic volumes: two variables whose influence

#473563 https://doi.org/10.1364/BOE.473563
Journal © 2022 Received 19 Aug 2022; revised 30 Sep 2022; accepted 1 Oct 2022; published 2 Nov 2022

Biomedical Optics EXPRESS

on the detectability of oxygen desaturation in tissue due to external pressure is scarcely studied. Noteworthy are studies on hematoma detectability [19,20]. While these studies are similar in nature and methodology, they distinguish themselves by the area of application, size of inclusion, and type of monitoring.

The aim of this paper is to determine the detectability of hypoxic volumes in human muscle and, consequently, the feasibility of a device to prevent PI.

2. Methods

2.1. Parameter selection

One of the most common algorithms used in NIRS is the Modified Beer-Lambert Law (MBLL; [21]), which relates changes in light attenuation to changes in chromophore concentrations. In Eq. (1), the MBLL defines the optical density OD as a logarithmic function of emitted light I_0 and a measurable light intensity I. By relating it with the i chromophore concentrations c_i, and their respective molar extinction coefficients (ε_i), present in the attenuating substance and is thus used to calculate changes of oxygenated (O_2Hb), deoxygenated (HHb) and total hemoglobin (tHb) concentration from changes in measured light intensity.

$$OD(t,\lambda) = -log_{10}(\frac{I(t,\lambda)}{I_0(t,\lambda)}) = \sum \varepsilon_i(\lambda) c_i DPF(\lambda) d + G(\lambda) \tag{1}$$

In Eq. (1), DPF stands for *differential path length factor*, which is used to scale the source-detector distance d to the actual path length of the light in the tissue. G is a scattering-dependent light intensity loss parameter, which can be neglected when calculating the change in optical density (see Eq. (2)) because the scattering properties μ_s are assumed to be constant.

$$\Delta OD(\Delta t,\lambda) = -log_{10}(\frac{I(t_1,\lambda)}{I(t_0,\lambda)}) = \sum \varepsilon_i(\lambda) \Delta c_i(\Delta t) DPF(\lambda) d \tag{2}$$

This equation describes the temporal changes of measured light intensity and, when considering two wavelengths λ, can be formulated as shown in Eq. (3), a principle that applies specifically for continuous-wave NIRS.

$$\begin{bmatrix} \Delta[HHb] \\ \Delta[O_2Hb] \end{bmatrix} = (d)^{-1} \begin{bmatrix} \varepsilon_{HHb,\lambda_1} & \varepsilon_{O_2Hb,\lambda_1} \\ \varepsilon_{HHb,\lambda_2} & \varepsilon_{O_2Hb,\lambda_2} \end{bmatrix}^{-1} \begin{bmatrix} \Delta OD(\Delta t,\lambda_1)/DPF(\lambda_1) \\ \Delta OD(\Delta t,\lambda_2)/DPF(\lambda_2) \end{bmatrix} \tag{3}$$

Clinically, however, the absolute tissue oxygen saturation (StO_2) is the value of interest. In order to measure it, the so-called spatially resolved spectroscopy (SRS) algorithm [22], which relates the spatial derivative of the measured OD to the optical properties of the specimen (Eq. (4)), is used.

$$\frac{\partial OD}{\partial r} = \frac{1}{\ln(10)}(\sqrt{3\mu_a \mu s'} + \frac{2}{r}) \tag{4}$$

From this spatial derivative, an absorption coefficient with an unknown scaling factor $k\mu_a$ can be calculated as shown in Eq. (5) [22]. In this equation, the reduced scattering coefficient μ_s' was replaced by $k(1-h\lambda)$, where h is a coefficient that is similar for different tissues and subjects [22].

$$k\mu_a(\lambda) = \frac{1}{3(1-h\lambda)}(\ln(10)\frac{\partial OD(\lambda)}{\partial r} - \frac{2}{r})^2 \tag{5}$$

Similarly to Eq. (3), the relative absorption coefficient $k\mu_a(\lambda)$ can be related to the relative hemoglobin concentrations $k[O_2Hb]$ and $k[HHb]$ by the molar extinction coefficients as shown

Biomedical Optics EXPRESS

in Eq. (6).

$$\begin{bmatrix} k[HHb] \\ k[O_2Hb] \end{bmatrix} = \begin{bmatrix} \varepsilon_{HHb,\lambda_1} & \varepsilon_{O_2Hb,\lambda_1} \\ \varepsilon_{HHb,\lambda_2} & \varepsilon_{O_2Hb,\lambda_2} \end{bmatrix}^{-1} \begin{bmatrix} k\mu_a(\lambda_1) \\ k\mu_a(\lambda_2) \end{bmatrix} \tag{6}$$

From these relative hemoglobin concentrations, StO_2 can be calculated, as the scaling factor k cancels out, as shown in Eq. (7).

$$StO_2 = \frac{[O_2Hb]}{[O_2Hb] + [HHb]} \tag{7}$$

The ability to calculate StO_2 will be crucial for a device to prevent pressure injuries. Equations (3) and (6) show the necessity of using at least two wavelengths to measure tissue oxygenation or changes thereof. However, all measurements and simulations in this work were performed at a single wavelength, based on the assumption that detectability of a hypoxic volume depends mainly on the difference in optical density between normal and hypoxic tissue, ΔOD, of the wavelength exhibiting the strongest difference of molar extinction of O_2Hb and HHb (see Fig. 1).

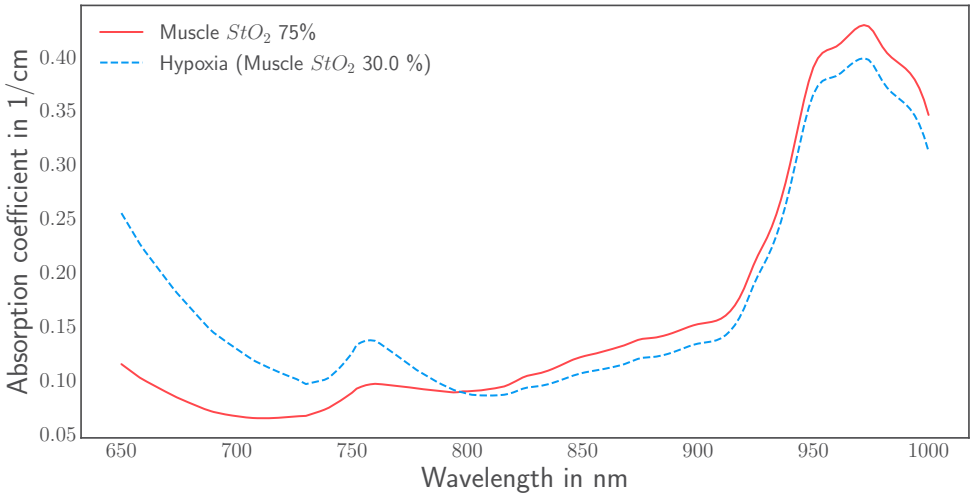

Fig. 1. Absorption spectra for normal and hypoxic muscle tissue model (curves are computed from published spectra of the molar extinction coefficients of $[O_2Hb]$ and $[HHb]$ [26]).

An assumed muscle tissue with StO_2 of 75%, such that $[O_2Hb] = 30\,\mu mol/l$, $[HHb] = 10\,\mu mol/l$ (concentrations in agreement with [23]), while containing 75% water is used for numerical studies. (These are the three main chromophores in the near-infrared spectrum; myoglobin has an almost identical absorption spectrum as hemoglobin and is therefore considered part of the hemoglobin spectrum [24]). The absorption spectrum of this theoretical tissue, as shown in Fig. 1, is in agreement with literature values for muscle [24] and also with measurements carried out by the authors of this study. The same figure shows the absorption spectrum of hypoxic muscle tissue.

StO_2 of hypoxic muscle tissue was chosen to be 30%. This value was found to be a reasonable estimate of poorly-oxygenated muscle according to the literature [22,25].

For this study, a wavelength of 700 nm was used. This wavelength in our theoretical model (Fig. 1) corresponds to values of 0.1 cm^{-1} for muscle (comparable to [24]) and 0.2 cm^{-1} for hypoxic muscle, constituting a change in absorption due to ischemia of 0.1 cm^{-1} (in agreement with [12]).

Biomedical Optics EXPRESS

The investigated hypoxic volumes were spherical in shape (compare Fig. 2) and chosen to be in the range of 1 to 6 cm^3. Even small hypoxic volumes (such as those which may develop locally under bony prominences [9]) may lead to harmful lesions and need to be detected early to prevent PI. Unfortunately, in contrast to the high prevalence of deep tissue injuries, research on this topic is scarce [27].

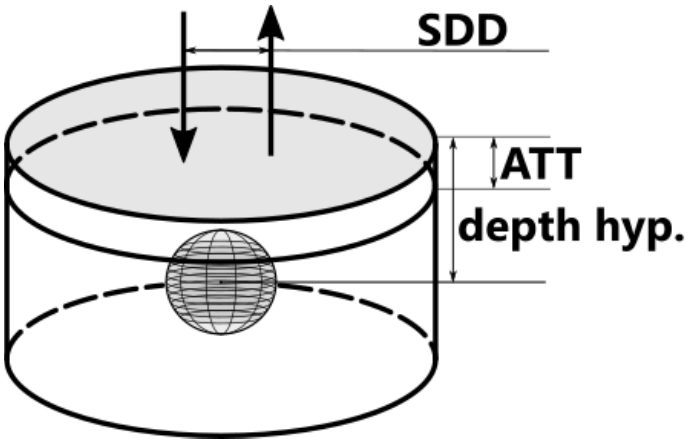

Fig. 2. Two-layer geometry with hypoxic volume used for computer simulations (ATT stands for adipose tissue thickness and SDD for source-detector distance).

Additionally, hypoxic volumes of 10, 20, and 30 cm^3 were considered to determine the magnitude of the influence of high ATT tissue configurations. The ranges of the depths (defined as length from model surface to center of hypoxic volume) of the hypoxic volumes (0.6 to 3 cm) and adipose tissue thicknesses (0.1 to 2 cm) were chosen such that their ranges covered the range of the physically relevant parameter space. Cases for which the combination of parameters, e.g., high ATT and low hypoxia depth, resulted in hypoxic volumes inside the AT-layer were omitted.

2.2. Computer simulations

Computer simulations were performed using the finite-element method (FEM), a frequently applied state-of-the-art tool for light-tissue interaction that is especially suitable when a large array of cases are to be evaluated. For this work a commercially available FEM software (COMSOL Multiphysics 5.5) was used.

FEM computations for light interaction in tissue are based on the diffusion approximation of the more extensive radiative transfer equation. For this study, the time-independent Eq. (8) was implemented.

$$\nabla \cdot (-D(\boldsymbol{r})\nabla\phi(\boldsymbol{r})) + \mu_a(\boldsymbol{r})\phi(\boldsymbol{r}) = S(\boldsymbol{r}) \tag{8}$$

In Eq. (8), $\phi(\boldsymbol{r})$ stands for the fluence rate in W/cm^2, $D(\boldsymbol{r})$ for the diffusion coefficient in cm and $\mu_a(\boldsymbol{r})$ for the absorption coefficient in cm^{-1} at coordinate $\boldsymbol{r}$. $S(\boldsymbol{r})$ denotes a time-independent continuous wave source.

The diffusion coefficient $D(\boldsymbol{r})$ is defined as shown in Eq. (9).

$$D(\boldsymbol{r}) = \frac{1}{3(\mu_a(\boldsymbol{r}) + \mu_s'(\boldsymbol{r}))} \tag{9}$$

μ_s' in Eq. (9) is the reduced scattering coefficient in cm^{-1}. To model a collimated beam, the source is implemented as a diffuse point source, located at $1/\mu_s'$ below the incident surface, with a power of 10 mW.

Biomedical Optics EXPRESS

To account for the internal reflection due to the refractive index mismatch of tissue (n$tissue$=1.4 [28]) and air (nair=1.0), a Robin boundary condition was employed on the top surface of the model (blue shaded in Fig. 2) as described in Eq. (10) [29].

$$\phi(\boldsymbol{r_s}) + 2Z\hat{\boldsymbol{n}} \cdot \nabla\phi(\boldsymbol{r_s}) = 0 \tag{10}$$

In Eq. (10), $\boldsymbol{r_s}$ are the boundary locations and $\hat{n}$ the outwards pointing normal vector to the boundary. Z is a parameter Keijzer et al. [30] derived from Fresnel's laws and corresponds to 2.74 for our case of reflective indexes. The different layers of tissue were considered to have the same index of refraction, and hence no reflection was implemented. This is a simplification: adipose tissue usually exhibits a slightly higher index of refraction than muscle tissue [31]; however Dehghani et al. [32] found that a significantly higher difference in indexes of refraction resulted in a negligible change in the amplitude of two-layer finite element simulations.

Additional studies were performed to eliminate the influence of meshing parameters.

Table 1 shows all parameters used in the finite element simulations.

Table 1. Parameters used in finite element computations.

Parameter	Value(s)	Remarks
SDD	$1.2 \cdots 5.2$ cm	Source-detector distance
ATT	$0.1 \cdots 1.9$ cm	Adipose tissue thickness
y	$0.2 \cdots 4$ cm	Depth hypoxia
V	$0.6 \cdots 30\,\text{cm}^3$	Volume hypoxia
$\mu_{a,f}$	$0.07\ \text{cm}^{-1}$	Absorption coefficient for adipose tissue
$\mu'_{s,f}$	$14.3\ \text{cm}^{-1}$	Reduced scattering coefficient for adipose tissue; from own measurements; in agreement with [13]
$\mu_{a,m}$	$0.1\ \text{cm}^{-1}$	Absorption coefficient for muscle tissue
$\mu'_{s,m}$	$6.8\ \text{cm}^{-1}$	Reduced scattering coefficient for muscle tissue from own measurements; in agreement with [13]
$\mu_{a,h}$	$0.2\ \text{cm}^{-1}$	Absorption coefficient for hypoxic muscle tissue
$\mu'_{s,h}$	$6.8\ \text{cm}^{-1}$	Reduced scattering coefficient for hypoxic muscle tissue from own measurements; in agreement with [13]
S	10 mW	Source strength
Z	2.74	Index mismatch parameter

2.3. Phantoms

Multi-layer phantoms were produced using silicone (Silpuran 2420 A/B, Wacker Chemie AG, Germany) and silicone-soluble color pastes Blue RAL 5022 and White RAL 9010 (Elastosil, Wacker Chemie AG, Munich, Germany), as well as carbon black powder (Alfa Aesar, Thermo Fisher GmbH, Karlsruhe, Germany). The manufacturing process and the color mixing calculations followed largely the procedure described by Tomm et al. [33].

To guarantee the same optical properties in all phantoms, a master blend for each emulated tissue type was mixed: Silpuran 2420 (component A) was mixed with the calculated amount of color paste (see Table 2). In those mixtures, the white color was responsible for the scattering properties, while the blue color was added to give the phantoms wavelength-dependent absorption properties, which was required for a different, unrelated project.

These master blends were then used to manufacture the individual phantoms. To evaluate the optical properties of all mixtures, precisely measurable single-layer phantoms were created.

Biomedical Optics EXPRESS

Table 2. Phantom color compositions for the three mimicked tissue types.

Phantom	Fat	Muscle	Hypoxia
$V_{\text{White RAL 9010}}$	1.48 µl/100 µl	0.74 µl/100 µl	0.68 µl/100 µl
$V_{\text{Blue RAL 5022}}$	-	-	1.85 µl/100 µl
$V_{\text{Carbon black}}$	0.71 µg/100 µl	1.65 µg/100 µl	1.52 µg/100 µl

2.3.1. Single-layer phantoms

To manufacture single-layer phantoms, the desired volume of the master blend was stirred thoroughly, and an equal amount of component B was added. The mixture was then poured into the molds and degassed until no more bubbles were visible. In a final step, the compound was heated up to 65°C to speed up the curing process. After 45 minutes, the solid phantoms were removed from the mold. After cooling down, the phantoms' optical properties were measured (see section 2.4.1). One single-layer phantom per tissue type (fat, muscle, hypoxic muscle) was manufactured.

2.3.2. Multi-layer phantoms

The multi-layer phantoms were manufactured similarly: first, one layer was mixed, stirred, and degassed before it was put in the oven to partially cure to a semi-solid state for about 15 minutes. The second layer was then poured on top of the first layer.

For phantoms with hypoxic inclusions, a mold with hemispherical shapes was used. After curing, two hemispheres of equal volume were then pulled on a thread in such a way that a sphere was formed. This threaded sphere was then placed inside the phantom molds at a pre-defined height and horizontal position and the desired layers were poured into the mold as described above.

A total of 6 multi-layer phantoms were manufactured: P1 (phantom without hypoxic inclusion), P1+ (phantom with hypoxic inclusion), P2, P2+, P3 and P3+. The phantoms' dimensions were 15 cm in diameter and 10 cm in height. The hypoxic inclusions were spherical in shape and ranged from 1.3 cm to 1.8 cm in diameter (see Table 4).

2.4. Phantom measurements

2.4.1. Measurements to determine bulk optical properties

After producing the phantoms, they were measured using an ISS Imagent (ISS Inc., Champaign, Illinois, USA) equipped with an absolute probe [34]. See Table 3.

Table 3. Optical properties resulting from phantom color compositions described in Table 2. Measured using an absolute probe of the ISS Imagent. A 5% error is considered for the ISS Imagent [33].

Phantom		Fat	Muscle	Hypoxia
ISS Imagent	$\mu_{a,725nm}$	0.068 ± 0.003 cm^{-1}	0.098 ± 0.005 cm^{-1}	0.196 ± 0.01 cm^{-1}
	$\mu'_{s,725nm}$	14.28 ± 0.71 cm^{-1}	6.78 ± 0.34 cm^{-1}	6.78 ± 0.34 cm^{-1}

2.4.2. Measurements to determine the influence of hypoxic volumes

Three phantom configurations (see Fig. 3) were measured; their properties are shown in Table 4. One phantom configuration consists of two silicone phantoms: a two-layer (fat and muscle) phantom with a hypoxic inclusion (e.g., P1+) and one without (e.g., P1).

Biomedical Optics EXPRESS

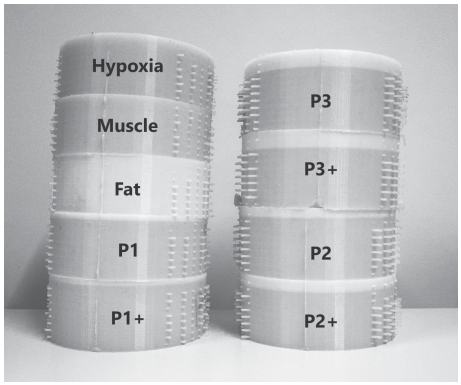

Fig. 3. Fabricated and measured phantoms.

Table 4. Geometrical properties of phantom configurations.

Phantom	P1	P2	P3
Adipose tissue thickness	0.3 cm	0.5 cm	0.7 cm
Hypoxia depth	1.2 cm	1.5 cm	2 cm
Hypoxia volume	1.2 cm^3	2.0 cm^3	3.0 cm^3

To measure the phantoms in a repeatable fashion, a measurement puck (see Fig. 4 was manufactured. In this puck, holes of two distinct diameters (to ensure fit for source and detector fibers, respectively) were drilled in a spiral shape. Such a shape ensures that measurements at all SDDs are centered with respect to the phantom. The detector and source fibers were connected to the ISS Imagent's PMT and laser diodes, respectively. The gain of the PMT was held constant throughout all measurements.

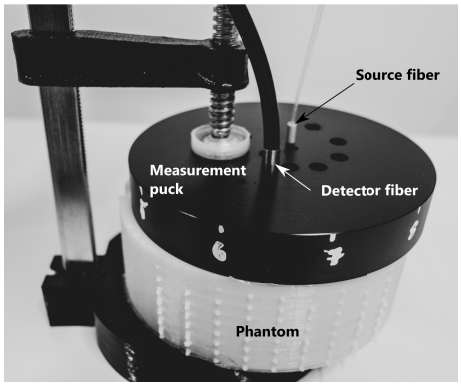

Fig. 4. Measurement set-up. The numbers mark angles of 36°.

The measurement procedure per phantom was as follows: The measurement puck was placed on the phantom to be measured and fixed using a clamp. The source and detector fibers were inserted into their corresponding borehole and slightly pushed into the phantom to ensure good contact between fiber and phantom. The resulting rebounding due to the phantom's elasticity should, in combination with the well-defined shaft-hub-tolerance, ensure a uniform contact pressure at all source and detector points. The phantom and puck were then covered with an

Biomedical Optics EXPRESS

opaque cloth, and the LED was switched on for 5 seconds, during which the PMT signal was recorded. After the measurement was completed, the source and detector fibers were removed from the puck and inserted into the corresponding holes for the next SDD, and the measurement was completed accordingly. After repeating this measurement process for all SDDs, the clamp was released, and the puck was rotated 36° before being clamped to the phantom again, after which the measurement process was repeated for all SDDs (1.2, 2.0, 2.8, 3.6, and 4.4 cm). For every measurement, it was made sure that the midpoint between source and detector was aligned with the phantom center axis.

This was performed 10 times until the measurements were repeated over the entire 2π surface of the phantom to reduce the impact of uneven layer thicknesses or imperfectly placed hypoxia.

For each SDD, the mean PMT signal of the 10 measured orientations around the 2π angle was calculated. The process was repeated for each phantom. For each SDD, the difference in optical density between each pair of phantoms (configuration) was calculated as shown in Eq. (11),

$$\Delta OD = log(\frac{\phi_{norm}}{\phi_{hypoxic}}) \tag{11}$$

where $\phi_{hypoxic}$ and ϕ_{norm} stand for the average measured fluence rate of the phantom with and without a hypoxic inclusion, respectively.

3. Results

3.1. Comparison of phantom measurements and computer simulations

The results of the calculated ΔOD values from the FEM simulations are shown in Fig. 5 and are compared against the experimentally measured values using silicone phantoms with

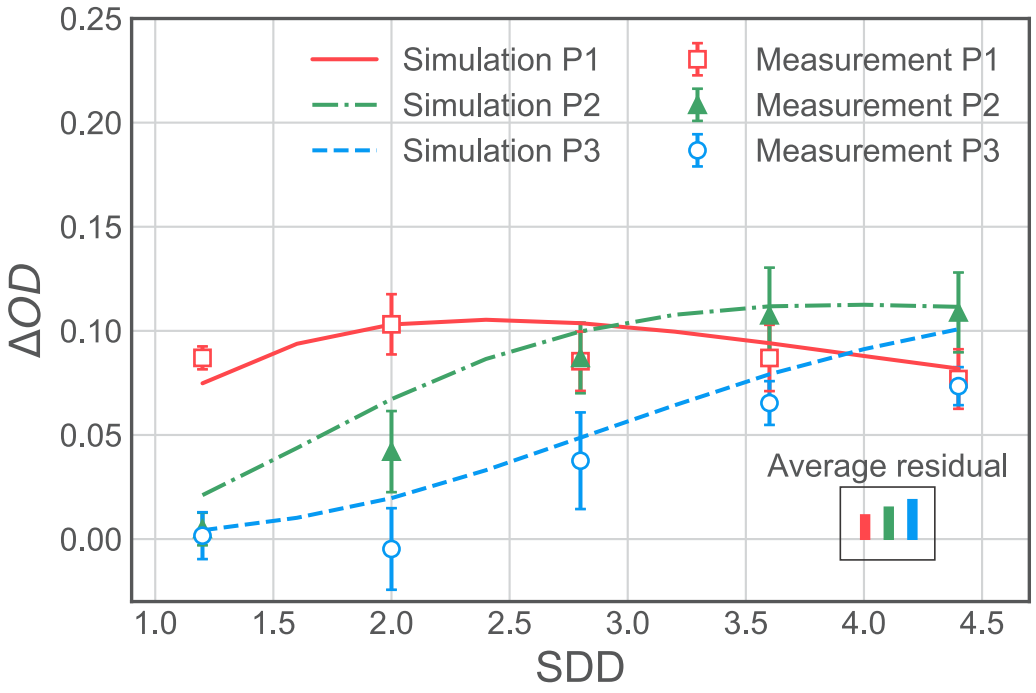

Fig. 5. Comparison of measurement with FEM simulations for three phantom configurations. Error bars stand for standard error. The average residual, plotted in the bottom right, is calculated as the mean of the difference of measurement and simulation at all SDD per phantom configuration.

Biomedical Optics EXPRESS

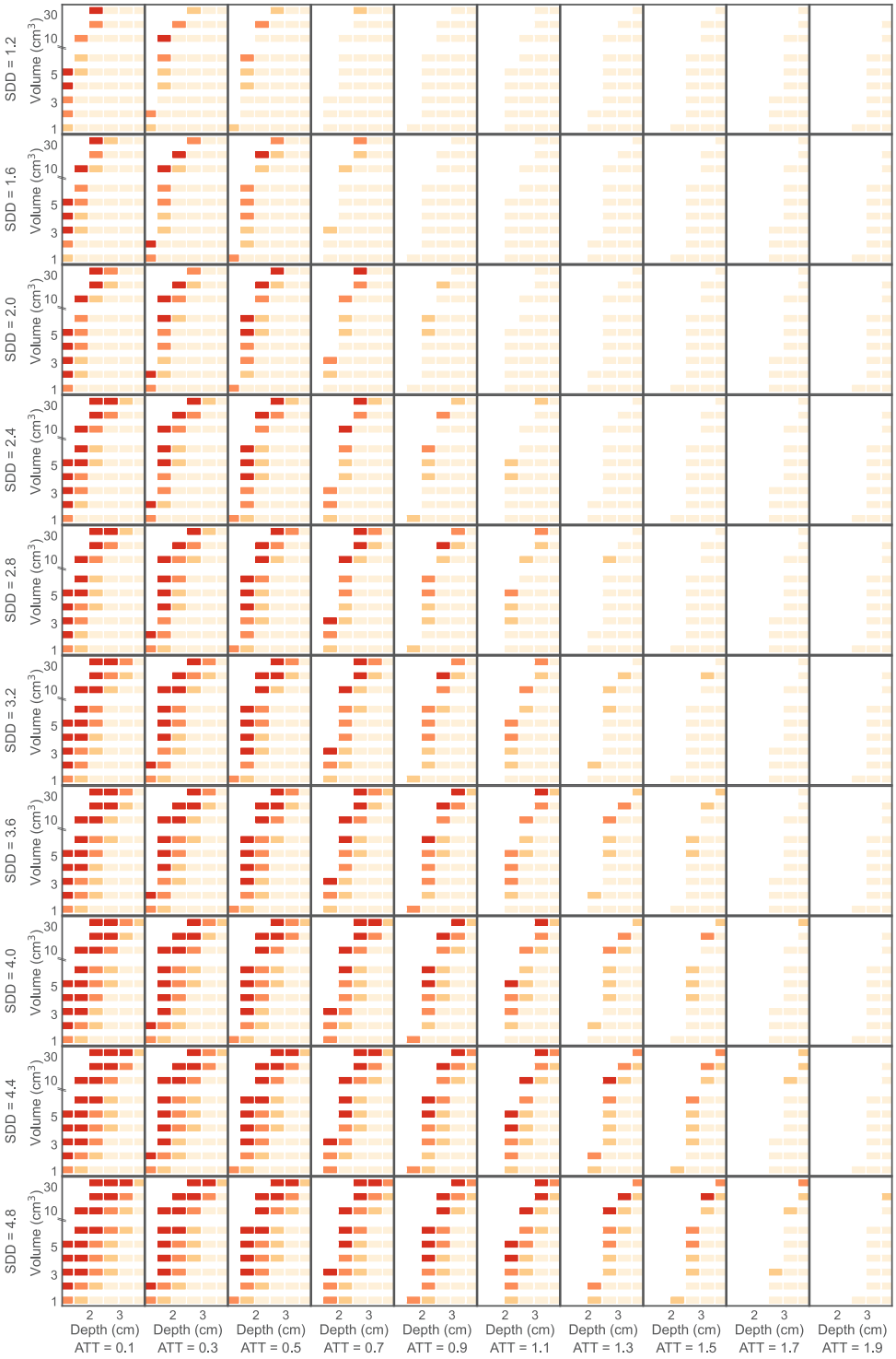

Fig. 6. Results of detectability of hypoxic volumes according to FEM computations. Red stands for highly detectable (ΔOD>0.1), orange for detectable (ΔOD>0.05), yellow for almost detectable (ΔOD>0.025) and light yellow for not detectable ($\Delta OD \leq 0.025$). If printed in grayscale, red appears darkest and light yellow lightest.

Biomedical Optics EXPRESS

configurations P1, P2, and P3. Average residuals for each configuration are shown as a means to quantify their experimental errors with a single value. To determine the expected repeatability of the measurements, the error is shown as the standard error of the mean. The average residuals for the phantom configurations P1, P2, and P3 are 0.0085, 0.0122, and 0.0158, respectively.

3.2. Detectability based on FEM computations

To assess the hypoxic volume detectability, a threshold ΔOD was chosen, taking hardware limits and other practical limitations into consideration. Figure 6 illustrates the entire set of FEM results with a detectability limit of $\Delta OD > 0.05$ (this limit was found to be sufficiently high not to trigger false positive detection of hypoxic volumes yet adequately low to detect hypoxic volumes for all investigated phantom configurations; compare Fig. 5).

Red and orange markers indicate detectable cases (cases in which the combination of a given phantom configuration and SDD resulted in an $\Delta OD \geq 0.05$), while yellow and light yellow markers mean undetectable ones. In each subplot, the vertical axis, displaying the hypoxic volume sizes, ranges from 1 cm^3 (top) linearly to 6 cm^3 (below the white line within the subplot). Above the white line, the excessive cases of 10, 20, and 30 cm^3 are displayed. The horizontal axis of each subplot represents the depth of the center of the hypoxic sphere below the surface and ranges from 0.6 cm to 3.7 cm. Each subplot represents a certain ATT-SDD combination, as shown along the vertical and horizontal major axes. The white space in each subplot represents the region where the radius of the embedded hypoxic sphere is greater than the hypoxic depth in the muscle and was therefore not simulated.

When omitting the extreme cases of 10, 20 and 30 cm^3, Fig. 6 shows a maximum detectable depth of 2.8 cm, a maximum ATT under which hypoxia can be detected of 1.5 cm and a minimal detectable hypoxic volume of 1.2 cm^3.

Figures 7 and 8 show the resulting difference in optical density as a function of SDD and hypoxic volume size, with the hypoxic volume positioned at 1.2 cm and 1.7 cm, respectively, below an ATT of 0.1 cm.

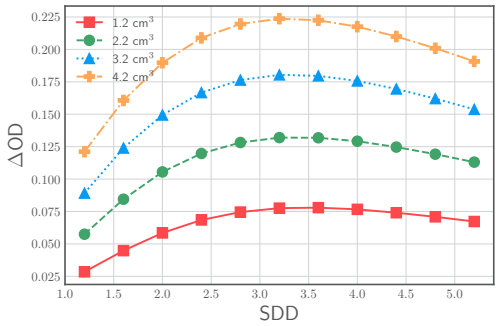

Fig. 7. Hypoxic volume placed at a depth of 1.2 cm. ATT of 0.1 cm.

Similarly, Figs. 9 and 10 depict the resulting differences in optical density as a function of ATT and hypoxic volume size, with the hypoxic volume positioned at a depth of 1.7 cm, using an SDD of 1.2 cm and 2.8 cm, respectively.

Biomedical Optics EXPRESS

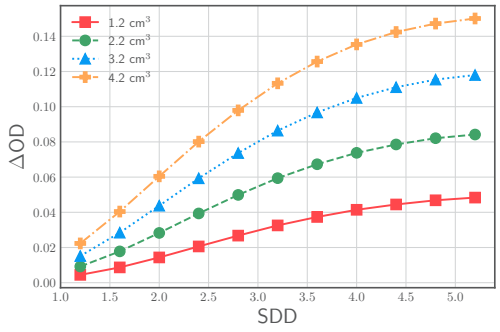

Fig. 8. Hypoxic volume placed at a depth of 1.7 cm. ATT of 0.1 cm.

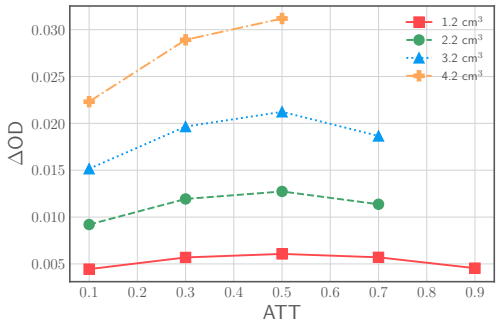

Fig. 9. Hypoxic volume placed at a depth of 1.7 cm. SDD of 1.2 cm.

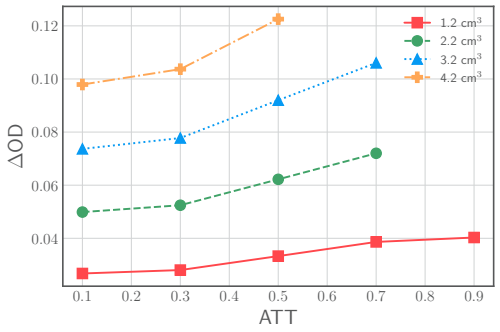

Fig. 10. Hypoxic volume placed at a depth of 1.7 cm. SDD of 2.8 cm.

4. Discussion

4.1. Comparison of phantom measurement and computer simulations

Upon visual inspection, Fig. 5 shows good agreement of the simulation results of the chosen phantom configuration with the respective measurements. This is confirmed by low residuals (the averages of which are plotted in Fig. 5) and thus affirms the correctness of how the FEM simulations are set up for this set of problems. For phantom configurations P2 and P3, the measurements show slightly lower ΔOD values than the simulations through all SDDs, while for the P1 configuration, the measurement values are centered around the simulation values. Interestingly, the residuals seem to increase with increasing ATT. This deviation can likely be

Biomedical Optics EXPRESS

explained by the measurement error (5-10%) of the device (see section 2.4.1) used to quantify the optical properties of manufactured phantoms. Shrinkage of hypoxic volume during the curing process and imprecision in the production of these volumes could constitute a minor contribution to this behavior. These volume-dependent variances would also explain the increasing residuals with increasing hypoxic volume.

The numerical results, represented by solid and dashed lines, show a self-similar shape. As ΔOD can be interpreted as a measure of sensitivity, one can see that each configuration has a defined sensitivity maximum and that with increasing hypoxia depth, this maximum is shifted to the right, and the peak prominence decreases.

4.2. Detectability based on FEM computations

Figure 6 shows the detectability of a wide range of cases. Most importantly, hypoxic volumes under adipose tissue layers of up to 1.7 cm are detectable. However, when excluding the excessive volumes (>6 cm^3), an ATT of 1.5 cm can be considered the detectability limit of hypoxic volumes.

A detectability limit for ATTs of 1.5 cm does not restrict the use of a potential device to prevent PI in obese people, because in a real-world application the hemoglobin in the adipose tissue is equally deoxygenated as in the muscle and hence, hypoxia is easily detected there. The reason is that, when e.g. sitting, the pressure between the bone and the skin is equally distributed along the vertical axis, likely resulting in one large hypoxic volume along this axis.

One interesting finding of our parameter study is the high detectability of small and shallow hypoxic volumes using intermediate and high SDDs. As depicted in Fig. 6, an SDD of 1.2 cm does not detect any case a higher SDD would not. This makes the inclusion of shorter SDDs for the purpose of hypoxia detection unnecessary. This phenomenon is shown in greater detail in Figs. 7 and 8. In the former, it is shown that for a given ATT and hypoxia depth, there exists an ideal SDD. In the latter, it is shown that for a hypoxia positioned at a depth of 1.7 cm, the theoretically ideal SDD can practically already not be realized due to SNR-related limitations of current devices.

Interestingly, something similar can be seen for the ATT. In Fig. 9, it is shown, that for a suboptimal SDD, there exists an "ideal" ATT. The decrease in sensitivity at higher ATT can be explained by the decreasing share of photons grazing the hypoxic volume of the muscle tissue (as described by [12]). In Fig. 10, the same configuration is shown with a higher SDD, which results in higher ΔOD values (due to higher sensitivity). Under these circumstances, it can be said that the higher the ATT, the higher the sensitivity to hypoxia. Most likely because a bigger share of the path the photons travel through is constituted by fat tissue, which exhibits a smaller absorption coefficient than muscle tissue.

Although the results of the phantom measurements in Fig. 5 match well with the FEM simulations, there are limitations to this study: the omission of noise and the resulting assumption of absolute hardware precision. While this assumption has proven to be applicable at short and intermediate SDDs, there are hardware-related limits at longer SDDs, plainly because not enough photons arrive at the detector to ensure a high enough signal-to-noise ratio. In the literature, this limit can be found to be around 4 cm [35], depending strongly on the kind of photon-detecting component.

The other limitation of the described method to determine detectability is the definition of a fixed ΔOD limit. This also depends on the used hardware and other factors, such as the employed algorithm and the integrating time for measurements. Our measurements (see Fig. 5) show however, that the chosen limit of 0.05 (see Fig. 6) is a reasonable estimate for such a limit.

Biomedical Optics EXPRESS

5. Conclusion

Our results show detectability of hypoxic volumes under adipose tissue thicknesses of up to 1.5 cm. The maximum tissue depth, at which hypoxic volumes could be detected was 2.8 cm. The smallest detectable hypoxic volume in our study was 1.2 cm^3.

Furthermore, finite element simulations show that a combination of mid- and long source-detector distances suffice to detect hypoxic volumes, even close to the surface, rendering the use of short SDDs redundant.

The shown detectability of hypoxic volumes proves the basic feasibility of a device built to raise an alarm in case of danger of PI development.

Funding. Innosuisse - Schweizerische Agentur für Innovationsförderung (20-B2-1_180983/1); Schweizerischer Nationalfonds zur Förderung der Wissenschaftlichen Forschung (20-B2-1_180983/1).

Acknowledgments. This work was supported by the Bridge Discovery grant no. 20-B2-1_180983/1 from the Swiss National Science Foundation and the Swiss Innovation Agency.

The authors thank Dr. Aldo di Costanzo Mata of the Biomedical Optics Research Laboratory at the Department of Neonatology of the University Hospital Zurich for advice on manufacturing the silicone phantoms and Prof. Martin Wolf for fruitful discussions.

Disclosures. The authors declare no conflicts of interest.

Data availability. Data underlying the results presented in this paper are not publicly available at this time but may be obtained from the authors upon reasonable request through a mutual agreement.

References

1. W. B. Mortenson, W. C. Miller and the SCIRE Research Team, "A review of scales for assessing the risk of developing a pressure ulcer in individuals with sci," Spinal Cord **46**(3), 168–175 (2008).
2. M. F. Cremasco, F. Wenzel, S. S. Zanei, and I. Y. Whitaker, "Pressure ulcers in the intensive care unit: the relationship between nursing workload, illness severity and pressure ulcer risk," J. Clin. Nurs. **22**(15-16), 2183–2191 (2013).
3. M. DeVivo and V. Farris, "Causes and costs of unplanned hospitalizations among persons with spinal cord injury," Top. Spinal Cord Inj. Rehabil. **16**(4), 53–61 (2011).
4. H.-G. Damert, F. Meyer, and S. Altmann, "Therapieoptionen bei Dekubitalulzera," Zentralbl. Chir. **140**(02), 193–200 (2015).
5. Y.-K. Jan, B. A. Crane, F. Liao, J. A. Woods, and W. J. Ennis, "Comparison of muscle and skin perfusion over the ischial tuberosities in response to wheelchair tilt-in-space and recline angles in people with spinal cord injury," Arch. Phys. Med. Rehabil. **94**(10), 1990–1996 (2013).
6. P. Bouyé, V. Jacquinandi, J. Picquet, F. Thouveny, J. Liagre, G. Leftheriotis, J.-L. Saumet, and P. Abraham, "Near-infrared spectroscopy and transcutaneous oxygen pressure during exercise to detect arterial ischemia at the buttock level: Comparison with arteriography," J. Vasc. Surg. **41**(6), 994–999 (2005).
7. G. Berg, S. Nyberg, P. Harrison, J. Baumchen, E. Gurss, and E. Hennes, "Near-infrared spectroscopy measurement of sacral tissue oxygen saturation in healthy volunteers immobilized on rigid spine boards," Prehospital Emerg. Care **14**(4), 419–424 (2010).
8. U. Källman, S. Bergstrand, A.-C. Ek, M. Engström, L.-G. Lindberg, and M. Lindgren, "Different lying positions and their effects on tissue blood flow and skin temperature in older adult patients: *Different lying positions effects on tissue blood flow and skin temperature*," J. Adv. Nurs. **69**(1), 133–144 (2013).
9. A. F. Mak, M. Zhang, and E. W. Tam, "Biomechanics of pressure ulcer in body tissues interacting with external forces during locomotion," Annu. Rev. Biomed. Eng. **12**(1), 29–53 (2010).
10. P. P. S. Mohammad, S. Isarangura, A. Eddins, and A. B. Parthasarathy, "Comparison of functional activation responses from the auditory cortex derived using multi-distance frequency domain and continuous wave near-infrared spectroscopy," Neurophotonics **8**(04), 1 (2021).
11. M. A. Franceschini, S. Fantini, L. A. Paunescu, J. S. Maier, and E. Gratton, "Influence of a superficial layer in the quantitative spectroscopic study of strongly scattering media," Appl. Opt. **37**(31), 7447 (1998).
12. L. Lin, M. Niwayama, T. Shiga, N. Kudo, M. Takahashi, and K. Yamamoto, "Two-layered phantom experiments for characterizing the influence of a fat layer on measurement of muscle oxygenation using NIRS," in *Infrared Spectroscopy: New Tool in Medicine*, vol. 3257 H. H. Mantsch and M. Jackson, eds., International Society for Optics and Photonics (SPIE, 1998), pp. 156–166.
13. M. Niwayama, L. Lin, J. Shao, N. Kudo, and K. Yamamoto, "Quantitative measurement of muscle hemoglobin oxygenation using near-infrared spectroscopy with correction for the influence of a subcutaneous fat layer," Rev. Sci. Instrum. **71**(12), 4571 (2000).
14. M. C. P. Van Beekvelt, M. S. Borghuis, B. G. M. Van Engelen, R. A. Wevers, and W. N. J. M. Colier, "Adipose tissue thickness affects in vivo quantitative near-IR spectroscopy in human skeletal muscle," Clin. Sci. **101**(1), 21–28 (2001).

Biomedical Optics EXPRESS

15. U. Wolf, M. Wolf, J. H. Choi, L. A. Paunescu, L. P. Safonova, A. Michalos, and E. Gratton, "Mapping of Hemodynamics on the Human Calf with Near Infrared Spectroscopy and the Influence of the Adipose Tissue Thickness," in *Oxygen Transport To Tissue XXIII*, vol. 510 D. F. Wilson, S. M. Evans, J. Biaglow, and A. Pastuszko, eds. (Springer US, Boston, MA, 2003), pp. 225–230.
16. Y. Yang, O. O. Soyemi, M. R. Landry, and B. R. Soller, "Influence of a fat layer on the near infrared spectra of human muscle: quantitative analysis based on two-layered monte carlo simulations and phantom experiments," Opt. Express **13**(5), 1570–1579 (2005).
17. S. Grieger, D. Geraskin, A. Steimers, and M. Kohl-Bareis, "Analysis of NIRS-based muscle oxygenation parameters by inclusion of adipose tissue thickness," in *Oxygen Transport to Tissue XXXV*, vol. 789 S. Van Huffel, G. Naulaers, A. Caicedo, D. F. Bruley, and D. K. Harrison, eds. (Springer New York, 2013), pp. 131–136. Series Title: Advances in Experimental Medicine and Biology.
18. V. M. Niemeijer, J. P. Jansen, T. van Dijk, R. F. Spee, E. J. Meijer, H. M. C. Kemps, and P. F. F. Wijn, "The influence of adipose tissue on spatially resolved near-infrared spectroscopy derived skeletal muscle oxygenation: the extent of the problem," Physiol. Meas. **38**(3), 539–554 (2017).
19. J. D. Riley, F. Amyot, T. Pohida, R. Pursley, Y. Ardeshipour, J. M. Kainerstorfer, L. Najafizadeh, V. Chernomordik, P. Smith, J. Smirniotopoulos, E. M. Wassermann, and A. H. Gandjbakhche, "A hematoma detector-a practical application of instrumental motion as signal in near infrared imaging," Biomed. Opt. Express **3**(1), 192 (2012).
20. J. Wang, J. Lin, Y. Chen, C. G. Welle, and T. J. Pfefer, "Phantom-based evaluation of near-infrared intracranial hematoma detector performance," J. Biomed. Opt. **24**(4), 1 (2019).
21. D. T. Delpy, M. Cope, P. v. d. Zee, S. Arridge, S. Wray, and J. Wyatt, "Estimation of optical pathlength through tissue from direct time of flight measurement," Phys. Med. Biol. **33**(12), 1433–1442 (1988).
22. S. Suzuki, S. Takasaki, T. Ozaki, and Y. Kobayashi, "Tissue oxygenation monitor using NIR spatially resolved spectroscopy," in *Optical Tomography and Spectroscopy of Tissue III*, vol. 3597 B. Chance, R. R. Alfano, and B. J. Tromberg, eds., International Society for Optics and Photonics (SPIE, 1999), pp. 582–592.
23. B. J. Lutjemeier, L. F. Ferreira, D. C. Poole, D. Townsend, and T. J. Barstow, "Muscle microvascular hemoglobin concentration and oxygenation within the contraction-relaxation cycle," Respir. Physiol. Neurobiol. **160**(2), 131–138 (2008).
24. R. M. P. Doornbos, R. Lang, M. C. Aalders, F. W. Cross, and H. J. C. M. Sterenborg, "The determination of in vivo human tissue optical properties and absolute chromophore concentrations using spatially resolved steady-state diffuse reflectance spectroscopy," Phys. Med. Biol. **44**(4), 967–981 (1999).
25. S. J. Matcher, P. J. Kirkpatrick, K. Nahid, M. Cope, and D. T. Delpy, "Absolute quantification methods in tissue near-infrared spectroscopy," in *Optical Tomography, Photon Migration, and Spectroscopy of Tissue and Model Media: Theory, Human Studies, and Instrumentation*, vol. 2389 (International Society for Optics and Photonics, 1995), pp. 486–495.
26. S. Prahl, Tabulated Molar Extinction Coefficient for Hemoglobin in Water (1998 (accessed December 3, 2020)).
27. A. Stekelenburg, D. Gawlitta, D. L. Bader, and C. W. Oomens, "Deep Tissue Injury: How Deep is Our Understanding?" Arch. Phys. Med. Rehabil. **89**(7), 1410–1413 (2008).
28. J. J. J. Dirckx, L. C. Kuypers, and W. F. Decraemer, "Refractive index of tissue measured with confocal microscopy," J. Biomed. Opt. **10**(4), 044014 (2005).
29. M. Schweiger, S. R. Arridge, M. Hiraoka, and D. T. Delpy, "The finite element method for the propagation of light in scattering media: Boundary and source conditions," Med. Phys. **22**(11), 1779–1792 (1995).
30. M. Keijzer, W. M. Star, and P. R. M. Storchi, "Optical diffusion in layered media," Appl. Opt. **27**(9), 1820 (1988).
31. I. Y. Yanina, E. N. Lazareva, and V. V. Tuchin, "Refractive index of adipose tissue and lipid droplet measured in wide spectral and temperature ranges," Appl. Opt. **57**(17), 4839 (2018).
32. H. Dehghani, B. Brooksby, K. Vishwanath, B. W. Pogue, and K. D. Paulsen, "The effects of internal refractive index variation in near-infrared optical tomography: a finite element modelling approach," Phys. Med. Biol. **48**(16), 2713–2727 (2003).
33. N. Tomm, L. Ahnen, H. Isler, S. Kleiser, T. Karen, D. Ostojic, M. Wolf, and F. Scholkmann, "Characterization of the optical properties of color pastes for the design of optical phantoms mimicking biological tissue," J. Biophotonics **12**(4), e201800300 (2019).
34. D. M. Hueber, S. Fantini, A. E. Cerussi, and B. B. Barbieri, "New optical probe designs for absolute (self-calibrating) NIR tissue hemoglobin measurements," in *Optical Tomography and Spectroscopy of Tissue III*, vol. 3597 B. Chance, R. R. Alfano, and B. J. Tromberg, eds., International Society for Optics and Photonics (SPIE, 1999), pp. 618–631.
35. F. Scholkmann, S. Kleiser, A. J. Metz, R. Zimmermann, J. Mata Pavia, U. Wolf, and M. Wolf, "A review on continuous wave functional near-infrared spectroscopy and imaging instrumentation and methodology," NeuroImage **85**, 6–27 (2014).